

Some simple rules for contrast, signal-to-noise and resolution in in-line x-ray phase-contrast imaging

Timur E. Gureyev*, Yakov I. Nesterets, Andrew W. Stevenson, Peter R. Miller, Andrew Pogany and Stephen W. Wilkins

CSIRO Materials Science and Engineering, Private Bag 33, Clayton South 3169, Australia

*Corresponding author: Tim.Gureyev@csiro.au

Abstract: Simple analytical expressions are derived for the spatial resolution, contrast and signal-to-noise in X-ray projection images of a generic phase edge. The obtained expressions take into account the maximum phase shift generated by the sample and the sharpness of the edge, as well as such parameters of the imaging set-up as the wavelength spectrum and the size of the incoherent source, the source-to-object and object-to-detector distances and the detector resolution. Different asymptotic behavior of the expressions in the cases of large and small Fresnel numbers is demonstrated. The analytical expressions are compared with the results of numerical simulations using Kirchhoff diffraction theory, as well as with experimental X-ray measurements.

©2008 Optical Society of America

OCIS codes: (340.7440) X-ray imaging; (100.2960) Image analysis; (110.2990) Image formation theory; (110.4980) Partial coherence in imaging.

References and links

1. R. Fitzgerald, "Phase-sensitive x-ray imaging," *Physics Today* **53**(7), 23-26 (2000).
2. A. Snigirev, I. Snigireva, V. Kohn, S. Kuznetsov, and I. Schelokov, "On the possibilities of x-ray phase contrast microimaging by coherent high-energy synchrotron radiation," *Rev. Sci. Instrum.* **66**, 5486-5492 (1995).
3. S. W. Wilkins, T. E. Gureyev, D. Gao, A. Pogany and A. W. Stevenson, "Phase-contrast imaging using polychromatic hard X-rays," *Nature* **384**, 335-338 (1996).
4. P. Cloetens, R. Barrett, J. Baruchel, J.-P. Guigay, and M. J. Schlenker, "Phase objects in synchrotron radiation hard x-ray imaging," *J. Phys. D: Appl. Phys.* **29**, 133-146 (1996).
5. A. Krol, J. C. Kieffer and E. Foerster, "Laser-driven x-ray source for diagnostic radiology. Applications of X-rays Generated from Lasers and Other Bright Sources," *Proc. SPIE* **3157**, 156-163 (1997).
6. T. A. Shelkovenko, D. B. Sinars, S. A. Pikuz, K. M. Chandler and D. A. Hammer, "Point-projection x-ray radiography using an X pinch as the radiation source," *Rev. Sci. Instrum.* **72**, 667-670 (2001).
7. C. J. Kotre, I. P. Birch and K. J. Robson, "Anomalous image quality phantom scores in magnification mammography: evidence of phase contrast enhancement," *British J. Radiol.* **75**, 170-173 (2002).
8. J. M. Cowley, *Diffraction Physics* (North-Holland, Amsterdam, 1975), Sec.3.4.2.
9. K. A. Nugent, T. E. Gureyev, D. F. Cookson, D. Paganin and Z. Barnea, "Quantitative phase imaging using hard X-rays," *Phys. Rev. Lett.* **77**, 2961-2964 (1996).
10. Ya. I. Nesterets, S. W. Wilkins, T. E. Gureyev, A. Pogany and A. W. Stevenson, "On the optimization of experimental parameters for x-ray in-line phase-contrast imaging," *Rev. Sci. Instrum.* **76**, 093706 (2005).
11. M. R. Teague, "Deterministic Phase Retrieval: a Green's Function Solution," *J. Opt. Soc. Am.* **73**, 1434-1441 (1983).
12. T. E. Gureyev and S. W. Wilkins, "On X-ray phase imaging with a point source," *J. Opt. Soc. Am. A* **15**, 579-85 (1998).
13. T. E. Gureyev, A. Pogany, D. M. Paganin and S. W. Wilkins, "Linear algorithms for phase retrieval in the Fresnel region," *Opt. Commun.* **231**, 53-70 (2004).
14. T. E. Gureyev, D. M. Paganin, A. W. Stevenson, S. C. Mayo and S. W. Wilkins, "Generalized eikonal of partially coherent beams and its use in quantitative imaging," *Phys. Rev. Lett.* **93**, 068103-1 - 068103-4 (2004).
15. T. E. Gureyev, Ya. I. Nesterets, D. M. Paganin, A. Pogany and S. W. Wilkins, "Linear algorithms for phase retrieval in the Fresnel region. 2. Partially coherent illumination," *Opt. Commun.* **259**, 569-580 (2006).

16. A. Krol, R. Kincaid, M. Servol, J.-C. Kieffer, Y. Nesterets, T. Gureyev, A. Stevenson, S. Wilkins, H. Ye, E. Lipson, R. Toth, A. Pogany, I. Coman, "Initial experimentation with in-line holography x-ray phase-contrast imaging with ultrafast laser-based x-ray source," *Proc. SPIE* **6510**, 65100L (2007).
17. J.-P. Guigay, "Fourier transform analysis of Fresnel diffraction patterns and in-line holograms," *Optik* **49**, 121-125 (1977).
18. A. Pogany, D. Gao and S. W. Wilkins, "Contrast and resolution in imaging with a microfocus X-ray source," *Rev. Sci. Instrum.* **68**, 2774-2782 (1997).
19. P. Cloetens, J.-P. Guigay, C. De Martino and J. Baruchel, "Fractional Talbot imaging of phase gratings with hard x rays," *Opt. Lett.* **22**, 1059-1061 (1997).
20. V. E. Cosslett and W. C. Nixon, "The X-Ray Shadow Microscope," *J. Appl. Phys.* **24**, 616-623 (1953).
21. G. Margaritondo and G. Tromba, "Coherence-based edge diffraction sharpening of x-ray images: a simple model," *J. Appl. Phys.* **85**, 3406-3408 (1999).
22. K. Levenberg, "A method for the solution of certain non-linear problems in least squares," *Quart. Appl. Math.* **2**, 164-168 (1944).
23. D. Marquardt, "An algorithm for least-squares estimation of nonlinear parameters," *SIAM J. Appl. Math.* **11**, 431-441 (1963).
24. S. Geller, "Parameter interaction in least squares structure refinement," *Acta Cryst.* **14**, 1026-1035 (1961).
25. J. S. Rollett, *Computing Methods in Crystallography* (Pergamon Press, Oxford, 1965).
26. W. C. Hamilton, "Significance tests on the crystallographic R factor," *Acta Cryst.* **18**, 502-510 (1965).
27. S. Brennan and P. L. Cowan, "A suite of programs for calculating X-ray absorption, reflection, and diffraction performance for a variety of materials at arbitrary wavelengths," *Rev. Sci. Instrum.* **63**, 850-853 (1992).
28. Y. Amemiya, K. Wakabayashi, H. Tanaka, Y. Ueno and J. Miyahara, "Laser-stimulated luminescence used to measure X-ray diffraction of a contracting striated muscle," *Science* **237**, 164-168 (1987).
29. Y. Amemiya, "Imaging plates for use with synchrotron radiation," *J. Synch. Rad.* **2**, 13-21 (1995).

1. Introduction

X-ray phase-contrast imaging is a rapidly developing technique that shows great promise in medical, scientific and industrial applications [1]. Among different types of X-ray phase-contrast imaging, the so-called in-line imaging method is the simplest in principle and the easiest in practical implementation [2-4]. It typically involves an X-ray source that can provide high degree of spatial coherence in the incident illumination, while high chromatic coherence is often not required [3]. Suitable sources that have been used in this imaging modality include synchrotron insertion devices [2, 4], microfocus laboratory sources [3], and more recently plasma X-ray sources generated either by high-power optical lasers [5] or X-pinch [6]. It has been shown that in-line phase-contrast imaging is capable of providing greatly enhanced image contrast compared to conventional absorption-based imaging, especially for hard X-rays (~10-100 keV) and samples consisting predominantly of low-Z chemical elements. As a consequence, this technique is considered particularly promising for medical diagnostic applications [3, 7].

It is well-known [8, 3, 9] that in-line X-ray phase contrast in the case of weakly absorbing samples and moderate propagation distances is proportional to the second derivatives (Laplacian) of the projected electron density distribution in the sample. As a consequence, this imaging method is particularly sensitive to edges and interfaces in the sample providing a natural edge-enhancement effect in the images. From the point of view of most applications this edge enhancement is considered the main advantage of the method. Therefore, it is particularly important to find quantitative dependencies of the degree of edge enhancement, which is conventionally characterised by suitably defined maximum image contrast, spatial resolution and signal-to-noise ratio in the vicinity of the geometric image of the edge, as a function of the relevant properties of the source, the sample, the detector and the imaging layout. Some results in this direction have been obtained previously (see e.g. [10] and references therein). However, the need still exists in simple analytical expressions describing the main characteristics of the images of edge-like features, which on one hand are general enough to cover most experimental conditions of interest, and on the other hand are simple enough to allow one to easily estimate the expected degree of edge enhancement without

resorting to computer simulations. The present paper aims at providing such simple formulae which can be used for rapid evaluation of in-line X-ray imaging conditions.

The structure of the paper is as follows. In the next section we derive analytical expressions for contrast, spatial resolution and signal-to-noise ratio (SNR) in in-line images of a generic phase edge. In the case of large Fresnel numbers (short propagation distances), the formulae are derived for both monochromatic and polychromatic incident radiation, while in the case of small Fresnel numbers (long propagation distances) only monochromatic incident radiation is treated. In section 3 we analyze the expressions describing the contrast, spatial resolution and SNR and present simple "rules" for estimation of these quantities in in-line images. Section 4 contains the results of numerical simulations verifying the accuracy of the proposed "rules", while in section 5 we describe the experimental tests performed with an in-line imaging system based on a laboratory micro-focus X-ray source and Imaging Plates. Finally, brief conclusions are given in section 6.

2. Analytical formulae for in-line phase contrast

In this section we derive analytical expressions for contrast, spatial resolution and SNR in in-line images of an edge-like feature in a non-absorbing object. We consider three different cases: (1) monochromatic incident radiation and short propagation distances; (2) polychromatic incident radiation and short propagation distances; and (3) monochromatic incident radiation and long propagation distances. We show that our analytical formulae obtained in these three different cases are consistent with each other, as well as with the expected qualitative physical behavior of X-ray image contrast in the relevant regimes.

Let a sample be located immediately before the "object" plane $z = 0$ transverse to the optic axis z (Fig. 1). The sample is illuminated by an X-ray beam emanating from an extended spatially incoherent source located near the point $z = -R_1$. We assume that the X-ray transmission through the sample can be characterised by the complex transmission function $Q(x, y, \nu)$, $Q \equiv \exp[i\varphi - \mu]$, where (x, y) are the Cartesian coordinates in the object plane and ν is the radiation frequency ($\nu = c / \lambda = kc / (2\pi)$, where k is the wavenumber). The transmitted beam is registered by a position-sensitive detector located immediately after the "detector" plane $z = R_2$.

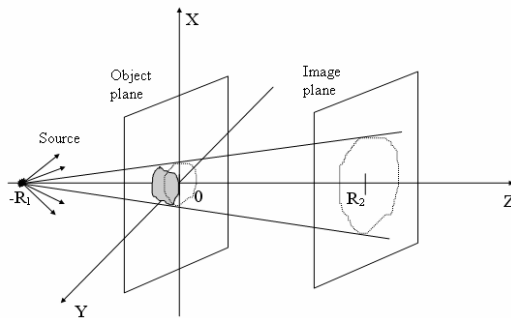


Fig. 1. In-line imaging geometry.

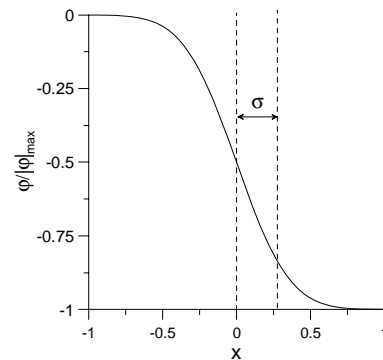


Fig. 2. Phase shift distribution in the object plane after transmission of the incident plane X-ray wave through a blurred phase edge.

Let us consider a simple but instructive example. Consider a generic edge-like feature in a non-absorbing sample ($\mu = 0$), in a vicinity of which the distribution of transmitted phase can be modeled as (Fig. 2)

$$\varphi(x, y, \nu) = -(H * P_{\text{obj}})(x) |\varphi|_{\text{max}}(\nu), \quad (1)$$

where the edge is assumed to be extended along the y coordinate, $|\varphi|_{\max}(\nu)$ is a constant representing the local maximum of the absolute value of the phase shift, $H(x)$ is the Heaviside "step" function (which is equal to 0 for negative x and is equal to 1 for positive x), $P_{\text{obj}}(x, y) = (2\pi\sigma_{\text{obj}}^2)^{-1} \exp[-(x^2 + y^2)/(2\sigma_{\text{obj}}^2)]$ is a function describing the "sharpness" of the edge and the asterisk denotes two-dimensional convolution.

Let $P_{\text{sys}}(x, y, M) = [2\pi\sigma_{\text{sys}}^2(M)]^{-1} \exp\{-(x^2 + y^2)/[2\sigma_{\text{sys}}^2(M)]\}$ be the point-spread function (PSF) of the imaging system referred to the object plane (we assume for simplicity that the PSF is the same at all X-ray energies), $\sigma_{\text{sys}}^2(M) = (M-1)^2 M^{-2} \sigma_{\text{src}}^2 + M^{-2} \sigma_{\text{det}}^2$ is the variance of the PSF, σ_{src} and σ_{det} are the standard deviations of the source intensity distribution and the detector PSF, respectively, and $M = (R_1 + R_2)/R_1$ is the geometric magnification. The particular form of the above expression for σ_{sys} is a direct consequence of the projection imaging geometry (Fig. 1).

2.1. Monochromatic near-field in-line contrast for a phase edge

It is well known that at sufficiently short propagation distances the spatial distribution of the spectral density, $S(x, y, z, \nu)$, in in-line images can be described by the Transport of Intensity equation (TIE) [8, 11, 12]. Let us substitute Eq. (1) into the monochromatic TIE for pure-phase objects [3, 12],

$$S(Mx, My, R_2, \nu) = M^{-2} S_{\text{in}}(\nu) [1 - (R'/k) \nabla^2 \varphi(x, y, \nu) * P_{\text{sys}}(x, y)], \quad (2)$$

where $S_{\text{in}}(\nu)$ is the spectral density of the incident beam, $S(x, y, R_2, \nu)$ is the spectral density distribution in the image plane $z = R_2$ and $R' = R_2/M$ is the effective propagation ("defocus") distance. As the derivative of the Heaviside function is the Dirac delta-function, we can write: $\nabla^2 \varphi * P_{\text{sys}} = -|\varphi|_{\max} \delta(x) * \partial_x (P_{\text{obj}} * P_{\text{sys}}) = x \exp[-x^2/(2\sigma_M^2)] |\varphi|_{\max} / (\sigma_M^3 \sqrt{2\pi})$, where $\sigma_M^2 \equiv \sigma_{\text{obj}}^2 + \sigma_{\text{sys}}^2(M)$. Substituting this expression into Eq. (2), we obtain

$$S(Mx, My, R_2, \nu) = M^{-2} S_{\text{in}}(\nu) \{1 - R'/(k\sigma_M^3 \sqrt{2\pi}) |\varphi|_{\max} x \exp[-x^2/(2\sigma_M^2)]\}. \quad (3)$$

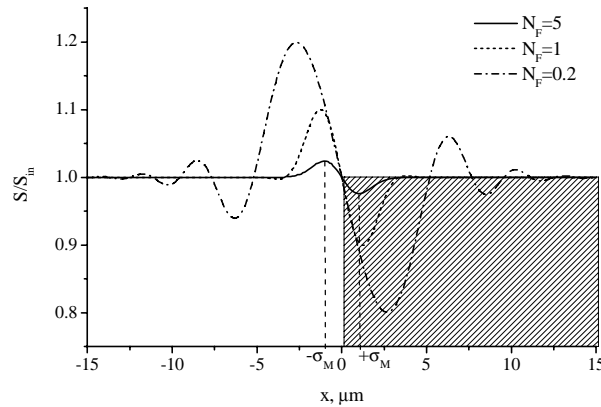


Fig. 3. Plot of the spectral density distribution in the vicinity of the geometric image of the edge feature for different values of the Fresnel number. The hatched area indicates the location of the object.

From Eq. (3) we can easily find the locations, $x = \pm\sigma_M$, of local maximum and minimum of the spectral density in the vicinity of an edge. These positions correspond to the centre of the "positive" and "negative" Fresnel fringes near the geometric shadow of the edge (Fig. 3) (note that the TIE allows for only one positive and one negative Fresnel fringe).

In the monochromatic case we define the image signal, $\Sigma(\nu, A)$, as the absolute value of the difference between the image spectral density distribution and the corresponding spectral density, $S_0(\nu) \equiv M^{-2} S_{\text{in}}(\nu)$, in the background image (without the edge feature), integrated over the area $A = 2Ma \times ML_y$ in the image plane, where L_y is the "length" of the edge feature in the object plane in the direction parallel to the edge and $(-a, a)$ is a vicinity of the edge along the x coordinate. Note that L_y is assumed to be sufficiently large (in particular, it is much larger than σ_{sys} and σ_{obj}). Using Eq. (3) we obtain:

$$\begin{aligned} \Sigma(\nu, A) &\equiv ML_y \int_{-Ma}^{Ma} |S(x', y', R_2, \nu) - S_0(\nu)| dx' = 2S_0(\nu) ML_y \frac{R'}{k} |\varphi|_{\text{max}}(\nu) \int_0^{Ma} \frac{x'}{M\sqrt{2\pi}\sigma_M^3} \\ &\times \exp\left(-\frac{x'^2}{2M^2\sigma_M^2}\right) dx' = 2S_{\text{in}}(\nu) L_y \frac{R'}{k\sigma_M\sqrt{2\pi}} |\varphi|_{\text{max}}(\nu) [1 - \exp(-\frac{a^2}{2\sigma_M^2})]. \end{aligned}$$

The noise is then calculated assuming the Poisson statistics as $N(\nu, A) = \sqrt{D(\nu, A)}$, where $D(\nu, A) = 4S_{\text{in}}(\nu)aL_y$ is the sum of the total X-ray spectral densities incident on the region of interest in the images with and without the edge feature. The SNR is then equal to,

$$SNR(\nu, A) = [S_{\text{in}}(\nu)L_y]^{1/2} \frac{R'}{k\sigma_M\sqrt{2\pi}} |\varphi|_{\text{max}}(\nu) a^{-1/2} [1 - \exp(-\frac{a^2}{2\sigma_M^2})].$$

It can be verified that $SNR(\nu, A)$ as a function of a reaches its maximum at $a \cong 2.162\sigma_M$. As the quantity $2\sigma_M$ is approximately equal to the width of the first Fresnel fringes in the TIE regime, it is natural to choose $a = 2\sigma_M$ for the calculation of the SNR corresponding to the phase contrast generated by the edge. Such a choice leads to almost maximal SNR, while also being convenient for practical evaluation of SNR in experimental phase-contrast images. We therefore define $SNR^{\text{TIE}}(\nu) \equiv SNR(\nu, 4M\sigma_M \times ML_y)$ and obtain:

$$SNR^{\text{TIE}}(\nu) = C_1 [D^{\text{TIE}}(\nu)]^{1/2} N_F^{-1} |\varphi|_{\text{max}}(\nu), \quad (4)$$

where $D^{\text{TIE}}(\nu) = 8S_{\text{in}}(\nu)\sigma_M L_y$ is the corresponding total incident X-ray spectral density, $N_F = \sigma_M^2 k / R'$ is the minimal Fresnel number (which corresponds to the size, $2\sigma_M$, of the smallest resolvable detail in the image [13]) and $C_1 = (1 - e^{-2}) / [4(2\pi)^{1/2}] \cong 0.0862$ is an absolute constant.

We define the maximum contrast in a region of an image as $C_{\text{max}}(\nu, A) = [S_{\text{max}}(\nu) - S_{\text{min}}(\nu)] / [S_{\text{max}}(\nu) + S_{\text{min}}(\nu)]$, where $S_{\text{max}}(\nu)$ and $S_{\text{min}}(\nu)$ are the maximum and minimum of the image spectral density in region A . Given the locations, $x = \pm\sigma_M$, of local maximum and minimum of spectral density in the vicinity of an edge and using Eq. (3) we obtain the following expression for the maximum contrast $C_{\text{max}}^{\text{TIE}}(\nu) \equiv C_{\text{max}}(\nu, 4M\sigma_M \times ML_y)$ inside the area $A = 4M\sigma_M \times ML_y$:

$$C_{\text{max}}^{\text{TIE}}(\nu) = C_2 N_F^{-1} |\varphi|_{\text{max}}(\nu) = C_3 SNR^{\text{TIE}}(\nu) [D^{\text{TIE}}(\nu)]^{-1/2}, \quad (5)$$

where $C_2 = (2\pi e)^{-1/2} \cong 0.2420$ and $C_3 = 4 / [e^{1/2}(1 - e^{-2})] \cong 2.806$ are absolute constants. Equation (5) describes the dependence of the contrast on such parameters as the wavelength

of the incident radiation, effective defocus distance and the spatial resolution of the imaging system. This equation indicates a very simple behavior of the image contrast in the TIE regime, i.e. the contrast is directly proportional to the maximum phase shift and to the inverse of the Fresnel number.

Equation (5) gives a convenient indicator of the validity of the TIE approximation that was used for its derivation. It is known [3, 12] that Eq. (2) is valid only if the corresponding image contrast is weak, i.e. $C_{\max}^{\text{TIE}}(\nu) \ll 1$, or, according to Eq. (5), $N_F \gg |\varphi|_{\max}(\nu)$. This necessary TIE validity condition is complementary to another commonly used necessary condition, $N_F \gg 1$, which does not depend on the magnitude of the phase shift. It was demonstrated in recent numerical simulations [13] that the TIE approximation does break down if one increases the maximum phase shift while keeping all other imaging parameters constant, therefore the condition $N_F \gg 1$ alone cannot be sufficient for the validity of the TIE. It is also easy to show that when $|\varphi|_{\max}(\nu) \ll 1$, the condition $N_F \gg |\varphi|_{\max}(\nu)$ is not sufficient for the validity of the TIE (see section 2.4 below). On the other hand, it is known that the TIE approximation is valid if and only if the transmission function satisfies the following condition: $|\nabla^2 Q(\mathbf{r}, \nu)| R' \lambda / \sigma_M \ll |\nabla Q(\mathbf{r}, \nu)|$, which allows one to use the first-order Taylor approximation for Q [13]. For the phase-edge object the latter condition is equivalent to $R' \lambda \max\{1, |\varphi|_{\max}(\nu)\} \ll \sigma_M \sigma_{\text{obj}}$. Therefore, the condition $N'_F \gg \max\{1, |\varphi|_{\max}(\nu)\}$, where $N'_F = 2\pi\sigma_M\sigma_{\text{obj}}/(R'\lambda)$, is necessary and sufficient for the validity of the TIE, Eq. (2). As, $\sigma_M \equiv [\sigma_{\text{obj}}^2 + \sigma_{\text{sys}}^2(M)]^{1/2} \geq \sigma_{\text{obj}}$, then $N_F \geq N'_F$, and the condition $N_F \gg \max\{1, |\varphi|_{\max}(\nu)\}$ is necessary, but not always sufficient for the validity of the TIE. In particular, an in-line image of a sharp edge (with a small σ_{obj}) may not be possible to adequately describe using the TIE, even if the spatial resolution of the imaging system is very low ($\sigma_{\text{sys}}(M)$ is large). Numerical simulations suggest that in such cases the convolution with the broad PSF of the imaging system may wash out high-order Fresnel fringes in the image, but the remaining first Fresnel fringe may become asymmetric, which obviously cannot be described by the TIE [10].

The spatial resolution of the imaging system shown in Fig. 1 can be conveniently estimated from the lateral spread of an image of a straight edge (for which $\sigma_{\text{obj}} \ll \sigma_{\text{sys}}$). For large Fresnel numbers N'_F the in-line image is described by Eq. (2), where the lateral spreading is obviously determined by the convolution with the PSF of the imaging system. If we exclude the influence of the object properties, then $\sigma_M = \sigma_{\text{sys}}(M)$ and we obtain the following expression for the finest achievable spatial resolution

$$(\Delta x)_{\min}^{\text{TIE}} = 2\sigma_{\text{sys}}(M) . \quad (6)$$

One can see that the TIE validity condition, i.e. $N'_F \gg \max\{1, |\varphi|_{\max}(\nu)\}$, imposes a limit on the spatial resolution consistent with the use of the TIE, Eq. (2). Indeed, it implies in particular that if $\sigma_{\text{obj}} \ll \sigma_{\text{sys}}$, then $\sigma_{\text{sys}} \gg \sqrt{R'\lambda}$. The expression $\sqrt{R'\lambda}$ is recognized as the width of the first Fresnel zone, which is also equal to the width of the first Fresnel fringe in an image of a sharp edge in an ideal imaging system with the delta-function-like PSF. In a system with the finite PSF width, $\sigma_{\text{sys}} > 0$, the width of Fresnel fringes depends on σ_{sys} as well. Note also that the TIE approximation allows for existence of only a single Fresnel fringe near the geometric image of an edge (this can be easily seen from the mathematical structure of Eq. (2)), so the spatial resolution of the TIE-based imaging is naturally associated with the width of the first Fresnel fringe. As will be shown explicitly in section 2.4 below, the width of the first Fresnel fringe reduces to the value given by Eq. (6) under the condition $\sigma_{\text{sys}} \gg \sqrt{R'\lambda}$, i.e. when $N_F \gg 1$.

Equation (6) also indicates that an improvement in the spatial resolution of in-line phase-contrast imaging in the TIE regime can only be achieved by deconvolving the system PSF from the registered images, which would allow one to eliminate (at least partially) the effect of the image blurring due to the finite source size and detector resolution.

2.2. Polychromatic near-field in-line contrast for a phase edge

In the case of polychromatic incident radiation and large Fresnel numbers, equations similar to Eqs. (4)-(6) can be obtained by integrating the spectral densities over the frequencies according to $I(x', y') = \int S(x', y', \nu) d\nu$, where I is the corresponding time-averaged intensity. The polychromatic TIE for pure phase objects is [14]

$$I(Mx, My, R_2) = M^{-2} I_{\text{in}} [1 - R' I_{\text{in}}^{-1} \nabla^2 \int S_{\text{in}}(\nu) k^{-1} \varphi(x, y, \nu) d\nu * P_{\text{sys}}(x, y)]. \quad (7)$$

Substituting the expression $\nabla^2 \varphi * P_{\text{sys}} = x \exp[-x^2 / (2\sigma_M^2)] |\varphi|_{\text{max}} / (\sigma_M^3 \sqrt{2\pi})$ into Eq. (7) and integrating over the area $4\sigma_M \times L_y$, we obtain the following expression for the signal-to-noise ratio in the polychromatic case:

$$SNR^{\text{TIE}} = C_1 (D^{\text{TIE}})^{1/2} \sigma_M^{-2} R' |\bar{\psi}|_{\text{max}}, \quad (8)$$

where $D^{\text{TIE}} = 8I_{\text{in}} \sigma_M L_y$ is the corresponding total incident X-ray intensity, $\bar{\psi} \equiv I_{\text{in}}^{-1} \int S_{\text{in}}(\nu) \varphi(\nu) k^{-1} d\nu$ is the "generalized eikonal" [14] of the transmitted polychromatic wave in the object plane, $|\bar{\psi}|_{\text{max}} \equiv I_{\text{in}}^{-1} \int S_{\text{in}}(\nu) |\varphi|_{\text{max}}(\nu) k^{-1} d\nu$ is the spectrally averaged maximum eikonal and $C_1 = (1 - e^{-2}) / [4(2\pi)^{1/2}] \cong 0.0862$ is an absolute constant.

As under the assumed approximations the positions, $x = \pm\sigma_M$, of the centre of the first Fresnel fringes are independent from the X-ray frequency, we can find an expression for the maximum image contrast from Eq. (7):

$$C_{\text{max}}^{\text{TIE}} = C_2 \sigma_M^{-2} R' |\bar{\psi}|_{\text{max}} = C_3 (D^{\text{TIE}})^{-1/2} SNR^{\text{TIE}}, \quad (9)$$

where $C_2 = (2\pi e)^{-1/2} \cong 0.2420$ and $C_3 = 4/[e^{1/2}(1 - e^{-2})] \cong 2.806$ are absolute constants. The corresponding TIE validity condition is $\sigma_M \sigma_{\text{obj}} / R' \gg \max\{\bar{\lambda}/(2\pi), |\bar{\psi}|_{\text{max}}\}$, where $\bar{\lambda} \equiv c I_{\text{in}}^{-1} \int S_{\text{in}}(\nu) \nu^{-1} d\nu$.

Equation (6) for the limit on the spatial resolution in TIE-based imaging remains valid in the polychromatic case.

2.3. Optimization of SNR in near-field in-line imaging

If one is interested in optimizing the conditions for X-ray in-line imaging in the sense of maximizing the SNR for an image of a phase edge at a fixed level of incident intensity, then, according to Eq. (8), one has to maximize the quantity

$$SNR^{\text{TIE}} = \gamma \frac{L_y^{1/2} R'}{\sigma_M^{3/2}} \int S_{\text{in}}(\nu) |\varphi|_{\text{max}}(\nu) k^{-1} d\nu, \quad (10)$$

where $\gamma \equiv (1 - e^{-2})(4\pi I_{\text{in}})^{-1/2}$ is a constant. We should emphasize that this formulation of the SNR optimization problem assumes that the incident intensity in the region of interest of the object plane is kept constant (this is generally consistent with the assumption of a fixed dose). This implies, for example, that if the source-to-object distance is varied from $R_1^{(0)}$

to $R_1^{(1)} = R_1^{(0)} + \Delta R_1$, then the exposure needs to be increased by the factor $(R_1^{(1)} / R_1^{(0)})^2$ provided that the source intensity stays the same, etc. For a given feature with fixed parameters σ_{obj} and L_y , the maximization can be achieved by improving the spatial resolution of the imaging system (decreasing $\sigma_{\text{sys}}(M)$), increasing the defocus distance R' and adjusting the incident spectrum in favor of the energies with larger values of $|\varphi|_{\text{max}}(\nu)/k$. If the incident spectrum is fixed as well and only the geometric parameters of the imaging system can be varied, then the quantity to be maximized is

$$SNR^{\text{TIE}} = \gamma' \frac{R'}{\sigma_M^{3/2}} = \gamma' \frac{R(M-1)}{M^{1/2} [M^2 \sigma_{\text{obj}}^2 + (M-1)^2 \sigma_{\text{src}}^2 + \sigma_{\text{det}}^2]^{3/4}}, \quad (11)$$

where $R = R_1 + R_2 = R_2 M / (M-1)$ is the total source-to-detector distance and $\gamma' = \gamma L_y^{1/2} \int S_{\text{in}}(\nu) |\varphi|_{\text{max}}(\nu) k^{-1} d\nu$ is a constant. Obviously, in the TIE regime this SNR monotonically increases as the source-to-detector distance R increases, or as the source size and detector PSF decrease. The only non-trivial dependence is that on magnification. Note that $SNR^{\text{TIE}}(M) = 0$ at both limits, $M = 1$ and $M = \infty$, according to Eq. (11). Therefore, the function $SNR^{\text{TIE}}(M)$ has a maximum at some intermediate value of magnification, $M = M_{\text{opt}}$, which can be found using Eq. (11).

Note that the optimal value of magnification will be independent of the total source-to-detector distance, and will be determined only by parameters σ_{obj} , σ_{src} and σ_{det} , i.e. by the sharpness of the edge, the X-ray source size and the spatial resolution of the detector system. It can be shown that when $\sigma_{\text{src}} = \sigma_{\text{det}}$, M_{opt} is always equal to 2. However, when $\sigma_{\text{src}} \neq \sigma_{\text{det}}$, M_{opt} can take different values. Consider, for example, the parameters used in our numerical and experimental tests later in this paper (these parameters correspond to an in-line system with a laboratory microfocus X-ray source and Imaging Plates as a detector), where $\sigma_{\text{src}} = 1.7 \mu\text{m}$ and $\sigma_{\text{det}} = 42.5 \mu\text{m}$. Then, taking e.g. $\sigma_{\text{obj}} = 0.7 \mu\text{m}$, one obtains from eq.(11) that $M_{\text{opt}} = 18$. On the other hand, under conditions more typical for synchrotron experiments, where one may have $\sigma_{\text{src}} = 42.5 \mu\text{m}$, $\sigma_{\text{det}} = 1.7 \mu\text{m}$, and assuming the same $\sigma_{\text{obj}} = 0.7 \mu\text{m}$, one obtains $M_{\text{opt}} = 1.059$. These values of the optimal magnification are fairly consistent with typical experimental experience.

The above results can be easily generalized further for the case of partially-coherent Schell-type incident illumination using the approach developed in [15].

It is also reasonably straightforward to account for X-ray absorption in the feature, provided the absorption is weak, so that the approximation $\exp[-2\mu_{\text{max}}(\nu)] \cong 1 - 2\mu_{\text{max}}(\nu)$ can be used at all frequencies ν present in the incident X-ray spectrum, where $2\mu_{\text{max}}(\nu)$ is the maximum X-ray attenuation in the feature [16].

2.4. Fresnel-region in-line contrast for a phase edge

In this section we derive analogues of Eqs. (4)-(6) in a more general form, which are not limited to the validity region of the TIE. Let the phase φ satisfy the Guigay condition [17]:

$$|\varphi(\mathbf{r}_+, \nu) - \varphi(\mathbf{r}_-, \nu)| \ll 1, \quad (12)$$

for all $\mathbf{r} = (x, y)$ in the object plane and all $\mathbf{r}_{\pm} = \mathbf{r} \pm (R'\lambda/2)\mathbf{p}$ with $\mathbf{p} = (\xi, \eta)$ from the circle B_{ρ} with the centre at the origin of coordinates in the Fourier space and radius ρ , $\rho = \min(\rho_{\text{sys}}, 2\rho_{\text{obj}})$, where ρ_{sys} and ρ_{obj} are the respective radii of the smallest circles outside which the Fourier transform of the system's PSF and the transmission function are negligibly small in magnitude. In the case of a plane monochromatic incident wave and the object plane

phase satisfying Eq. (12), the 2D spatial Fourier transform of the spectral density in the detector plane, $\hat{S}(\xi, \eta, R_2, \nu) = \iint \exp[-i2\pi(x\xi + y\eta)]S(x, y, R_2, \nu)dx dy$, can be expressed in the following form [15, 17]:

$$\hat{S}(\xi/M, \eta/M, R_2, \nu) = S_{\text{in}}(\nu) \{ \delta(\xi, \eta) + \sin[\pi\lambda R'(\xi^2 + \eta^2)] \hat{\phi}(\xi, \eta, \nu) \hat{P}_{\text{sys}}(\xi, \eta, M) \}, \quad (13)$$

where we also assumed for simplicity that $\hat{P}_{\text{sys}}(0, 0, M) = 1$. This equation represents a generalization of Eq. (2), with Eq. (2) formally obtainable from Eq. (13) by means of replacing the sine function by its argument followed by the inverse Fourier transform. The main advantage of Eq. (13) over Eq. (2) is that Eq. (13) is not limited to the "near-field", i.e. the condition $N'_F \gg \max\{1, |\varphi|_{\text{max}}(\nu)\}$ is not necessary for the validity of Eq. (13). Instead, Eq. (13) can be derived under condition (12) which effectively allows the phase function to consist of two components, one of them being large in magnitude, but slowly varying, with the second one being small in magnitude, but possibly rapidly varying [13]. Let us consider the small rapidly varying component first. The function $\varphi_0(x, y) = \varepsilon \sin(x/\sigma)$, with such parameters ε and σ that $\varepsilon \ll \sigma^2/(R'\lambda) \leq N'_F < 1$, obviously satisfies condition (12), because $|\varphi_0(x, y)| \leq \varepsilon \ll 1$. Therefore, the in-line phase contrast, including the Talbot effect, for the latter function can be described by Eq. (13) [19]. On the other hand, it is obvious that such effects cannot be generally described by Eq. (2). Thus, for the small phase functions, such that $|\varphi|_{\text{max}}(\nu) \ll 1$, the condition $N'_F \gg |\varphi|_{\text{max}}(\nu)$ is not sufficient for the validity of the TIE. Now consider the large slowly varying component of a phase function satisfying condition (12). For such functions condition (12) implies that $N'_F \gg |\varphi|_{\text{max}}(\nu)$. Moreover, by definition the spatial Fourier spectrum of the slowly varying component is confined to a small circle, $B_{\rho_{\text{obj}}}$, around the origin of coordinates in the Fourier space, such that $\rho_{\text{obj}}^2 \ll 1/(R'\lambda)$, hence $N'_F \gg 1$. In this case the sine function in Eq. (13) can be replaced by its argument, and Eq. (13) reduces to the TIE, Eq. (2). These examples agree well with the statement presented earlier in this paper that the necessary and sufficient condition for the validity of the TIE can be expressed as $N'_F \gg \max\{1, |\varphi|_{\text{max}}(\nu)\}$.

Having confirmed that Eq. (13) represents a non-trivial extension of Eq. (2), we proceed with deriving explicit expressions for the spatial resolution, contrast and SNR in in-line images of the edge-like feature defined by Eq. (1) under conditions (12). Substituting Eq. (1) into Eq. (13) and taking inverse Fourier transform we obtain that

$$S(Mx, My, R_2, \nu) = M^{-2} S_{\text{in}}(\nu) \{ 1 - |\varphi|_{\text{max}}(\nu) \sqrt{2n_F/\pi} F[x/(\sigma_M n_F), N_F] \}, \quad (14)$$

$$F(x, N_F) = \int_0^x \exp(-t^2/2) \sin[(1/2) \arctan N_F^{-1} - t^2/(2N_F)] dt, \quad (15)$$

where $n_F = \sqrt{1 + N_F^{-2}}$ and we used the fact that $F(\infty, N_F) = 0$ (the latter fact can be easily understood in the context of Eq. (14), if one considers the energy conservation requirement together with the obvious property $F(x, N_F) = -F(-x, N_F)$). Typical profiles of the spectral density in the vicinity of a geometric image of the edge calculated in accordance with Eqs. (14)-(15) are shown in Fig. 3 for the following values of the relevant parameters: $M = 1$, $|\varphi|_{\text{max}} = 1$, $\sigma_M = 1 \mu\text{m}$, $N_F = 0.2, 1$ and 5 .

The locations, x_m , of local maxima and minima of the spectral density are defined by the equation $(\partial_x F)[x_m/(\sigma_M n_F), N_F] = 0$, i.e. $x_m^\pm = \pm \sigma_M n_F \sqrt{N_F (2\pi m + \arctan N_F^{-1})}$,

$m = 0, \pm 1, \pm 2, \dots$. The locations of the first extrema to the left and right of the edge are $x_0^\pm = \pm \sigma_M \sqrt{(N_F + N_F^{-1}) \arctan N_F^{-1}}$, hence the width of first Fresnel fringe is approximately $\Delta x = 2\sigma_M \sqrt{(N_F + N_F^{-1}) \arctan N_F^{-1}}$. Excluding the contribution of the sample unsharpness function, P_{obj} , we obtain an expression for the limit of spatial resolution,

$$(\Delta x)_{\min} = 2\sigma_{\text{sys}}(M) \sqrt{(N_F + N_F^{-1}) \arctan N_F^{-1}}. \quad (16)$$

Note that the above definition of spatial resolution assumes that the higher-order Fresnel fringes are sufficiently weak to be neglected, and thus the spatial resolution is determined primarily by the width of the first Fresnel fringe. When $N_F \gg 1$, then $\arctan N_F^{-1} \cong N_F^{-1}$ and we obtain from Eq. (16) that $(\Delta x)_{\min} \cong 2\sigma_{\text{sys}}(M)$, which gives the limit of the spatial resolution for a sharp edge as defined by Eq. (6). At the opposite limit, when $N_F \ll 1$, then $\arctan N_F^{-1} \cong \pi/2$ and we obtain another well-known result [20, 18],

$$(\Delta x)_{\min}^{\text{far}} = 2\sigma_{\text{sys}}(M) \sqrt{(\pi/2) N_F^{-1}} = \sqrt{R'\lambda}. \quad (17)$$

Equation (17) also implies that at small Fresnel numbers a significant improvement in spatial resolution can potentially be achieved using phase retrieval, i.e. by numerically reconstructing the distribution of transmitted phase in the object plane from the registered intensity distribution in the image plane [13, 15].

As before, we define the local contrast in the vicinity of the edge as the ratio of the difference and the sum of spectral densities at the first maximum and minimum. Note that this definition of contrast assumes that the higher-order Fresnel fringes are weaker than the first fringe, and thus the local contrast is determined by the first Fresnel fringe. Taking into account Eq. (14) and the expression for x_0^\pm given above, we obtain the following expression for the contrast:

$$C_{\max}(\nu) = \sqrt{2/\pi} (1 + N_F^{-2})^{1/4} F(\sqrt{N_F \arctan N_F^{-1}}, N_F) |\varphi|_{\max}(\nu). \quad (18)$$

For large values of the Fresnel number we have $N_F \arctan N_F^{-1} \rightarrow 1$, $\sin[(1/2) \arctan N_F^{-1} - t^2 / (2N_F)] \cong (1 - t^2) / (2N_F)$, and taking into account the value of the definite integral $\int_0^1 \exp(-t^2/2)(1 - t^2) dt = e^{-1/2}$, we obtain that the expression given by Eq. (18) for $N_F \gg 1$ coincides with that given by Eq. (5). At the opposite end, when $N_F \ll 1$, we have $N_F \arctan N_F^{-1} \rightarrow \pi N_F / 2$, and taking into account the value of the definite integral $\int_0^1 \sin[(\pi/4)(1 - t^2)] dt \cong 0.4876$, we obtain that when $N_F \rightarrow 0$, the contrast asymptotically tends to the constant value

$$C_{\max}^{\text{far}}(\nu) = 0.4876 |\varphi|_{\max}(\nu). \quad (19)$$

We define the signal as above, i.e. as the absolute value of the difference between the image intensity distribution and the corresponding flat field intensity, $S_0(\nu) \equiv M^{-2} S_{\text{in}}$, integrated over the area corresponding to the first Fresnel fringes:

$$\begin{aligned}\Sigma &\equiv ML_y \int_{2Mx_0^-}^{2Mx_0^+} |S(x', y', \nu) - S_0(\nu)| dx = S_{\text{in}}(\nu) L_y |\varphi|_{\text{max}}(\nu) \sqrt{8n_F/\pi} \int_0^{2x_0^+} |F[x/(\sigma_M n_F), N_F]| dx \\ &= S_{\text{in}}(\nu) L_y |\varphi|_{\text{max}}(\nu) \sigma_M \sqrt{8n_F^3/\pi} \int_0^{2\sqrt{N_F} \arctan N_F^{-1}} |F(t, N_F)| dt.\end{aligned}$$

The corresponding Poisson noise is $N = \sqrt{D(\nu)}$, where $D(\nu) = 8x_0^+ L_y S_{\text{in}}(\nu)$ is the incident X-ray spectral density integrated over the area corresponding to the first Fresnel fringe in the images with and without the edge feature. The signal-to-noise, $SNR \equiv \Sigma/N$, is then equal to

$$SNR(\nu) = \alpha_{N_F} [D(\nu)]^{1/2} |\varphi|_{\text{max}}(\nu), \quad (20)$$

where $\alpha_{N_F} = n_F^{1/2} (8\pi N_F \arctan N_F^{-1})^{-1/2} \int_0^{2\sqrt{N_F} \arctan N_F^{-1}} |F(t, N_F)| dt$ is a positive value depending only on the Fresnel number. Therefore, the signal-to-noise is directly proportional to the square root of the integrated X-ray intensity incident on the feature and to the maximum phase shift produced by the feature. It can be easily verified that for large values of the Fresnel number, $\alpha_{N_F} \cong (1 - e^{-2})/[4(2\pi)^{1/2} N_F]$, and hence Eq. (20) coincides with Eq. (4). When $N_F \rightarrow 0$, then $\alpha_{N_F} \rightarrow (1/4) \int_0^2 \int_0^x \sin[(\pi/4)(1-t^2)] dt dx \cong 0.1325$, and Eq. (20) reduces to

$$SNR^{\text{far}}(\nu) \cong 0.1325 [D^{\text{far}}(\nu)]^{1/2} |\varphi|_{\text{max}}(\nu) \cong 0.2717 C_{\text{max}}^{\text{far}}(\nu) [D^{\text{far}}(\nu)]^{1/2}, \quad (21)$$

where $D^{\text{far}}(\nu) = 4S_{\text{in}} L_y \sqrt{R'\lambda}$. Therefore, the quantity

$$\gamma(N_F) \equiv SNR(\nu) [D(\nu)]^{-1/2} C_{\text{max}}^{-1}(\nu), \quad (22)$$

tends to approximately 0.2717 when $N_F \rightarrow 0$. One can see from Eq. (5) that $\gamma(N_F) \rightarrow e^{1/2}(1 - e^{-2})/4 \cong 0.3564$ when $N_F \rightarrow \infty$. We have calculated numerically the value of $\gamma(N_F)$ for a wide range of Fresnel numbers and found that $\gamma(N_F)$ varies slowly in between the two limits, 0.2717 and 0.3564.

One can obtain analogues of the above equations for the contrast, spatial resolution and signal-to-noise in the polychromatic case integrating the spectral density over the frequencies according to $I(x, y) = \int S(x, y, \nu) d\nu$. The polychromatic analogue of Eq. (14) is the following equation for the time-averaged intensity of a projection image of a pure-phase edge feature:

$$M^2 I(Mx, My, R_2) = I_{\text{in}} - \int S_{\text{in}}(\nu) |\varphi|_{\text{max}}(\nu) \sqrt{2n_F/\pi} F[x/(\sigma_M n_F), N_F] d\nu. \quad (23)$$

However, unlike the TIE case considered above, here the dependence on the wavelength ($\lambda = c/\nu$) cannot be generally factored out, unless the spectrum is so narrow that the dependence of $N_F = 2\pi\sigma_M^2/(R'\lambda)$ on ν can be neglected. In the latter case it is trivial to obtain exact analogues of Eqs. (16)-(21) with the maximum monochromatic phase shift, $|\varphi|_{\text{max}}(\nu)$, replaced by its average value over the spectrum, $|\varphi|_{\text{max}} = \int S_{\text{in}}(\nu) |\varphi|_{\text{max}}(\nu) d\nu / I_{\text{in}}$. If such a simplification is impossible, the dependence of contrast and other image parameters on the wavelength spectrum may become rather complicated [18].

3. Simple rules for estimation of contrast, SNR and spatial resolution

In this section we analyze the expressions obtained in the previous section for the contrast, SNR and spatial resolution in in-line images of non-absorbing edge-like feature, and suggest some simple rules for evaluation of these principal image parameters.

The graph of the value of $(\Delta x)_{\min} / (2\sigma_{\text{sys}})$ as a function of the inverse of Fresnel number calculated in accordance with Eq. (16) is presented in Fig. 4. As one can see from Fig. 4, the resolution values tend to a finite limit equal to $2\sigma_{\text{sys}}(M)$ for large Fresnel numbers in agreement with Eq. (6), while for small Fresnel numbers the spatial resolution becomes proportional to the square root of the inverse Fresnel number, eq.(17), which corresponds to a straight line in the logarithmic plot. Furthermore, one can see that the following "rule of thumb", which simply combines Eq. (6) and Eq. (17) and gives a reasonably good approximation for the spatial resolution of in-line imaging across a large range of Fresnel numbers.

Rule 1 (spatial resolution). The spatial resolution in in-line imaging of a phase edge-like feature satisfying Eq. (12) can be estimated as the largest of the two values, namely the width of the PSF of the imaging system, $2\sigma_{\text{sys}}(M)$, and the width of the first Fresnel zone, $\sqrt{R'\lambda}$.

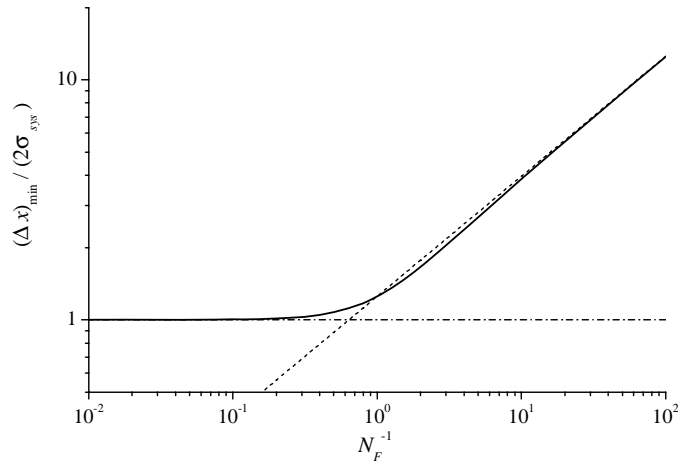


Fig. 4. Plot of the spatial resolution in in-line imaging as predicted by Eq. (16) (solid line), Eq. (17) (dotted line) and Eq. (6) (dash-dotted line).

The graph of the value of $C_{\max}(\nu) / |\varphi|_{\max}(\nu)$ as a function of the inverse of Fresnel number calculated in accordance with Eq. (18) is presented in Fig. 5. One can see that the image contrast as a function of the inverse Fresnel number displays a behavior which is complementary to that of the spatial resolution, i.e. at large Fresnel numbers the image contrast is directly proportional to the inverse Fresnel number in agreement with Eq. (5), while at small Fresnel numbers the contrast asymptotically converges to a constant value in accordance with Eq. (19).

The behavior illustrated by Fig. 4 and Fig. 5 indicates the existence of a trade-off between the image contrast and resolution as a function of inverse Fresnel number, i.e. as a function of the wavelength of the radiation, effective propagation distance and the width of the PSF of the imaging system. Therefore, the issue of optimization of experimental conditions in in-line imaging becomes important and non-trivial [18, 21, 10]. However, one can see that the

following "rule of thumb", which simply combines Eq. (5) and Eq. (19), gives a reasonably good approximation for the contrast of an in-line image of a phase edge across a large range of Fresnel numbers.

Rule 2 (image contrast). The maximum contrast in an in-line image of a phase edge-like feature satisfying Eq. (12) can be estimated as the product of the maximum absolute phase shift generated by the feature, $|\varphi|_{\max}(v)$, and the smallest of the two values, $0.2420/N_F$ and 0.4876.

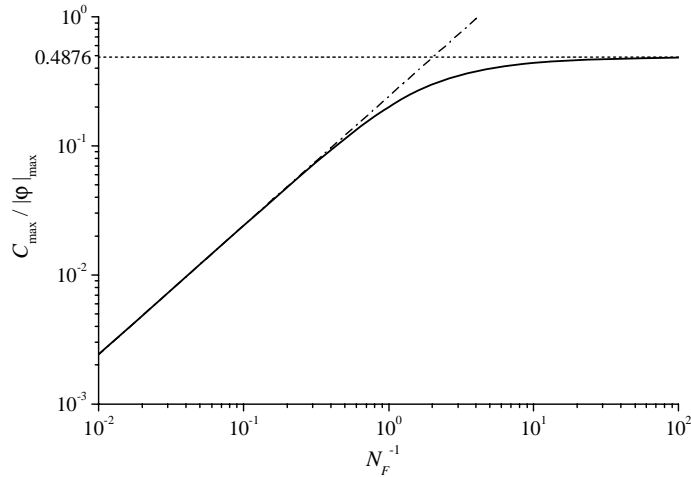


Fig. 5. Plot of the maximum image contrast in in-line imaging as predicted by Eq. (18) (solid line), Eq. (19) (dotted line) and Eq. (5) (dash-dotted line).

The graph of the value of $\gamma(N_F)$ calculated in accordance with Eq. (22) is presented in Fig. 6.

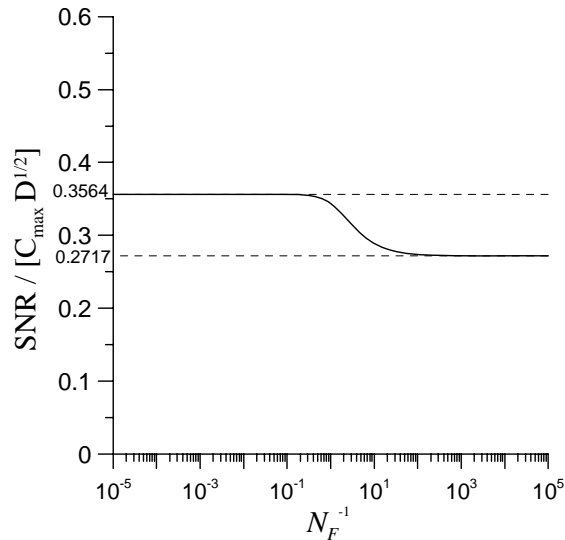


Fig. 6. Plot of the ratio of the SNR to the product of the maximum image contrast and the square root of the integral X-ray intensity incident on the region of interest.

One can see from Fig. 6 that $\gamma(N_F)$ varies slowly in between its two limits, 0.2717 and 0.3564, i.e. it does not change significantly over the full range of Fresnel numbers. Therefore, we can formulate the following "rule of thumb".

Rule 3 (signal-to-noise). The signal-to-noise in an in-line image of a phase edge-like feature satisfying Eq. (12) can be estimated as the product of approximately 0.3 times the image contrast (see Rule 2) and the square root of twice the integrated X-ray intensity incident on the feature.

4. Numerical results

In this section we present results of numerical simulation of in-line image contrast for a pure phase edge obtained using the Kirchhoff diffraction theory. These results are compared with the predictions given by the analytical formulae derived in section 2 above. For reader's convenience, the following table summarizes the validity conditions required for various imaging regimes considered below.

Table 1. Validity conditions for various approximations.

Approximation	Validity condition
"Exact" (Kirchhoff diffraction theory)	$R' \gg \lambda$
"TIE" (Transport of Intensity equation)	$R' \gg \lambda$, $R' \lambda \max\{1, \varphi _{\max}(\nu)\} \ll \sigma_M \sigma_{\text{obj}}$
"WO" (Weak object approximation)	$R' \gg \lambda$, $ \varphi(\mathbf{r}_+, \nu) - \varphi(\mathbf{r}_-, \nu) \ll 1$
"Far" (WO in the far Fresnel region)	$R' \gg \lambda$, $ \varphi(\mathbf{r}_+, \nu) - \varphi(\mathbf{r}_-, \nu) \ll 1$, $N_F \ll 1$

As the simulated sample we used an edge of a polyethylene (C_2H_4 , density = 1 g/cm^3) sheet of thickness $100 \mu\text{m}$, with the unsharpness parameter $\sigma_{\text{obj}}=0.7 \mu\text{m}$. The source was modeled as an X-ray tube with a tungsten anode operated at $E_p=50 \text{ kVp}$, and with 0.3 mm thick Be window. We also assumed that the lower X-ray energies were filtered out using a 1 mm thick Al filter. The normalized X-ray spectrum incident on the sample is shown in Fig. 7.

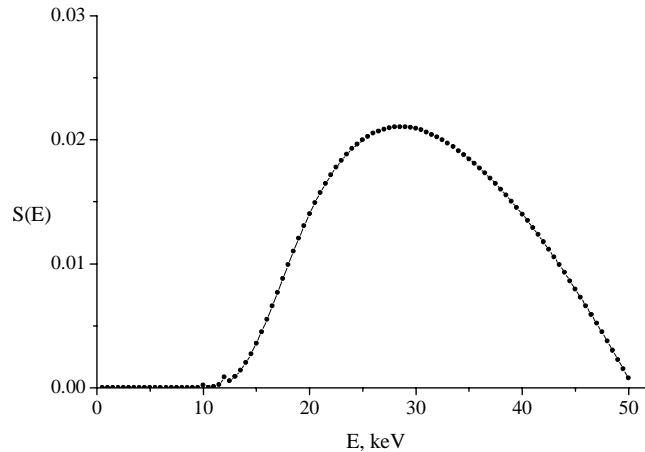


Fig. 7. Incident X-ray spectrum used to calculate the values in Tables 2 and 3.

The maximum absolute value of the generalized eikonal corresponding to the chosen sample and the X-ray spectrum was found to be equal to $|\bar{\psi}|_{\max} = 0.2947 \text{ \AA}$. The source size was assumed 4 \mu m (FWHM), the detector resolution was 100 \mu m (FWHM). We modeled an X-ray system with a fixed source-to-detector distance $R=2 \text{ m}$. In the simulations we changed the value of magnification (M) by changing the source-to-object distance, the effective defocus distance R' was changing accordingly. The comparison between the results obtained by simulating the images with the help of Kirchhoff integrals and those obtained using the analytical formulae (Eqs. (6), (8) and (9)) derived in the preceding sections are presented in Tables 2 and 3. It is easy to see that the agreement between the two sets of results is quite good, with the accuracy of the analytical results improving as the necessary validity condition for the TIE, $\sigma_M \sigma_{obj} / R' \gg \max\{\bar{\lambda}/(2\pi), |\bar{\psi}|_{\max}\}$, becomes better satisfied.

Table 2. Comparison of the image characteristics obtained with Kirchhoff diffraction theory ("Exact ") and those obtained using analytical formulae derived in the present paper, Eqs. (6), (8)-(9) ("TIE"), using $I_{in} = 10 \text{ ph}/\mu\text{m}^2$, $L_y = 1 \text{ mm}$ and $R = 2 \text{ m}$. The source size was 4 \mu m (FWHM) and the detector resolution was 100 \mu m (FWHM).

M	$\frac{\sigma_M \sigma_{obj}}{R' \bar{\psi} _{\max}}$	N_F	$R', \text{ mm}$	Contrast, %		Resolution, μm		SNR	
				Exact	TIE	Exact	TIE	Exact	TIE
2	1.01	142.0	500	0.76	0.79	43.28	42.52	3.54	3.67
5	0.641	36.6	320	2.81	3.06	17.81	17.26	8.44	9.07
10	0.603	18.2	180	5.60	6.15	9.48	9.14	12.30	13.26
25	0.76	12.3	76.8	8.46	9.08	5.08	4.91	13.56	14.34
50	1.209	16.0	39.2	6.78	7.02	4.06	3.99	9.75	10.0
100	2.244	27.8	19.8	3.98	4.04	3.77	3.74	5.51	5.56

Table 3. Comparison of the image characteristics obtained with Kirchhoff diffraction theory ("Exact ") and those obtained using analytical formulae derived in the present paper, Eqs. (6), (8)-(9) ("TIE"), using $I_{in} = 10 \text{ ph}/\mu\text{m}^2$ and $L_y = 1 \text{ mm}$ and $R = 2 \text{ m}$. The source size was 100 \mu m (FWHM) and the detector resolution was 4 \mu m (FWHM).

M	$\frac{\sigma_M \sigma_{obj}}{R' \bar{\psi} _{\max}}$	N_F	$R', \text{ mm}$	Contrast, %		Resolution, μm		SNR	
				Exact	TIE	Exact	TIE	Exact	TIE
1.32	0.672	46.2	367.3	2.23	2.42	21.43	20.80	7.38	7.87
1.16	0.607	24.4	237.8	4.18	4.59	12.59	12.16	10.59	11.41
1.08	0.621	14.7	137.2	6.94	7.61	7.44	7.17	13.51	14.52
1.04	0.775	12.4	74.0	8.46	9.06	4.99	4.83	13.47	14.18
1.02	1.229	16.2	38.4	6.70	6.93	4.05	3.98	9.62	9.85
1.01	2.265	28.0	19.6	3.94	4.00	3.76	3.74	5.46	5.51

In the next set of calculations we compared the results of analytical formulae, Eqs. (16), (18) and (20), with the corresponding results obtained using Kirchhoff diffraction theory, under the conditions corresponding to a broad range of Fresnel numbers including the small ones, where Eqs. (6)-(9) based on the TIE approximation are no longer valid. Here we used monochromatic incident radiation with energy $E = 30.78 \text{ keV}$ (the average energy of the spectrum in Fig. 7), $\lambda = 0.4 \text{ \AA}$. Compared to the first set of calculations, we also decreased the value of the maximum phase shift to $|\varphi|_{\max} = 1 \text{ rad}$ (which corresponds to the thickness of polyethylene of 25.66 \mu m) in order to satisfy conditions (12) across the whole considered range of Fresnel numbers. We kept the magnification constant at $M = 25.3$, which led to the

constant value of the standard deviation of the system PSF, $\sigma_{\text{sys}} = 2.341 \mu\text{m}$. The propagation distance was varied between 2 m and 1024 m, which corresponded to the Fresnel numbers between 12.28 and 0.024. The corresponding results are presented in Table 4. In the same table we also present for comparison the results obtained with Eqs. (9) and (6) (large Fresnel numbers, or TIE approximation), and with Eqs. (17) and (19) (small Fresnel numbers). One can see that Eqs. (16) and (18) give the values which agree very well with the results obtained using Kirchhoff diffraction theory across the whole considered range of Fresnel number values. As expected, the results given by Eqs. (6) and (9) and Eqs. (16) and (19) agree well with the Kirchhoff diffraction results for large and small Fresnel numbers, respectively. One can also easily verify that the simple Rules 1 and 2 formulated above give rather good estimation of the spatial resolution and contrast, respectively, in the considered examples.

Table 4. Comparison of the image contrast and spatial resolution obtained with Kirchhoff diffraction theory ("Exact") with those obtained using analytical formulae derived in the present paper. Analytical results are given for the general formulae, Eq. (16) and (18) ("WO"), as well as for the limiting cases of very large Fresnel numbers, Eq. (5) and Eq. (6) ("TIE") and very small Fresnel numbers, Eq. (17) and (19) ("Far"). The source size was $4 \mu\text{m}$ (FWHM), the detector resolution was $100 \mu\text{m}$ (FWHM), $\lambda = 0.4 \text{ \AA}$, $|\phi|_{\text{max}} = 1 \text{ rad}$ and $M = 25.3$.

$R, \text{ m}$	$R', \text{ m}$	N_F	Contrast, %				Resolution, μm			
			Exact	WO	TIE	Far	Exact	WO	TIE	Far
2	0.08	12.28	1.96	1.97	1.97	48.76	4.90	4.90	4.89	1.75
4	0.15	6.14	3.90	3.92	3.94		4.94	4.93		2.47
8	0.30	3.07	7.61	7.68	7.88		5.08	5.06		3.50
16	0.61	1.54	14.10	14.37	15.76		5.51	5.49		4.95
32	1.22	0.768	23.24	23.88	31.53		6.72	6.74		6.99
64	2.43	0.384	32.28	33.33	63.05		9.19	9.30		9.89
128	4.86	0.192	38.67	40.15	126.11		13.19	13.36		13.99
256	9.72	0.096	42.35	44.21	252.22		18.98	19.26		19.78
512	19.44	0.048	44.23	46.42	504.43		27.18	27.58		27.98
1024	38.88	0.024	45.21	47.58	1008.87		38.71	39.28		39.57

5. Experimental results

In order to further test some of the formulae presented here we performed X-ray imaging experiments with an object consisting of two sheets of $100 \mu\text{m}$ thick polyethylene. These sheets were overlapped and the edges (vertical and horizontal) crossed on the optic axis of the X-ray imaging instrument. The sheets in the sample were arranged in a crossed fashion in order to enable testing of the images of the vertical as well as the horizontal edges. The X-rays were produced by a Feinfocus FXE-225.20 microfocus source with a cylindrical W reflection-based target and $250 \mu\text{m}$ Be window. The source was operated at 30 kVp and $50 \mu\text{A}$. The source-to-object distance R_1 and object-to-detector distance R_2 were varied, but $R = R_1 + R_2$ was fixed at 2 m (magnification $M = R / R_1$). The detector was Fuji Imaging Plates ($20 \text{ cm} \times 25 \text{ cm}$; FDL-URV), scanned with a Fuji BAS-5000 scanner (using $25 \mu\text{m}$ pixel size). Under these experimental conditions, the object yielded images which possessed both absorption and phase contrast, but were dominated by the latter in the form of characteristic single black-white fringes (a typical image is presented in Fig.8). The images were subjected to flat-field correction and then analysed to provide contrast and resolution values. The observed (experimental) contrast values were obtained from the difference between the maximum and minimum intensity values divided by the sum of these quantities; the observed resolution values were obtained from the spatial separation of lines of maximum and minimum intensity, referred to the object plane. The observed data values, in both vertical and horizontal directions, are listed in Table 5.

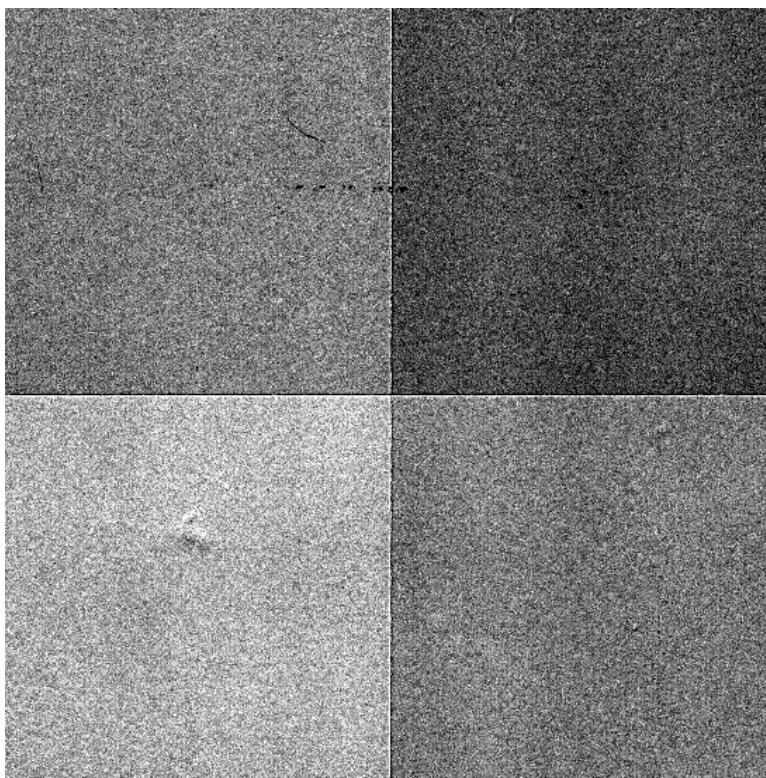


Fig. 8. An image of a phantom used in the experimental tests acquired at $R_1 = 10$ cm.

Table 5. Observed and calculated (corresponding to refined parameters in least-squares analysis) values of contrast and resolution, for both vertical and horizontal directions.

R_1 , cm	R_2 , cm	N_F	C_{obs} , %	C_{calc} , %	$(\Delta x)_{obs}$, μm	$(\Delta x)_{calc}$, μm
vertical						
5	195	32.1	6.9 (0.5)	5.7	10.0 (1.0)	9.2
10	190	19.2	9.6 (0.4)	9.5	10.0 (1.0)	9.9
20	180	16.0	10.7 (0.4)	11.4	13.0 (1.0)	12.4
40	160	22.3	9.3 (0.3)	8.1	20.0 (1.0)	19.6
60	140	34.1	7.5 (0.2)	5.3	27.0 (4.0)	27.8
horizontal						
5	195	40.2	4.9 (0.3)	4.5	9.0 (2.0)	10.3
10	190	23.1	7.5 (0.4)	7.8	10.0 (1.0)	10.9
20	180	17.8	8.4 (0.3)	10.2	13.0 (1.0)	13.2
40	160	23.2	7.3 (0.5)	7.8	20.0 (1.0)	20.0
60	140	34.6	5.6 (0.4)	5.2	29.0 (3.0)	28.0

The analysis of the experimental data in Table 5 was performed by non-linear least-squares refinement using a modification of the Levenberg-Marquardt algorithm [22, 23]. The experimental data is interpreted in terms of Eq. (5) for the contrast values and using $2\sigma_M$ for

the resolution values, i.e. monochromatic formulae. Correlation matrices and estimated standard deviations (esds) for refined-parameter values were calculated [24, 25], as was Hamilton's R-factor R_H [26] as a measure of agreement between theory and experiment. All of the observations (contrast and resolution) were weighted equally in the analysis. A total of six parameters could be refined (although the limited data set and correlations between parameters precluded all six being varied simultaneously): σ_{obj} ; $\sigma_{src}(vert)$; $\sigma_{src}(horiz)$; σ_{det} ; effective X-ray energy E ; polyethylene-sheet thickness t . Whilst the σ -values associated with the object and the detector could justifiably be treated as being the same in both vertical and horizontal directions, this was not true for the X-ray source (see below) and so two parameters were required.

Table 6. Refined parameter values from least-squares analysis of experimental data. Values in italics (and without an esd) were fixed. The values in square brackets are expressed as FWHM rather than σ (FWHM $\approx 2.35\sigma$) for convenience. R_H is Hamilton's R-factor and provides a measure of the agreement between theory and experiment [26].

σ_{obj} , μm	$\sigma_{src}(vert)$, μm	$\sigma_{src}(horiz)$, μm	σ_{det} , μm	E, keV < λ , \AA >	$ \varphi _{max}$, rad	t, μm	R_H , %
<i>4.0</i> [9.4]	2.0 (0.6) [4.7 (1.3)]	3.1 (0.4) [7.3 (1.0)]	44 (1) [104 (2)]	14.7 (0.4) <0.84 (0.05)>	7.54 (0.38)	<i>100</i>	6.8

Table 6 provides the parameter values obtained by a least-squares refinement in which the blur of the polyethylene edges was fixed at $\sigma_{obj} = 4 \mu\text{m}$ and the thickness was fixed at $t = 100 \mu\text{m}$. This value of σ_{obj} was arrived at by trial-and-error and, inasmuch as the corresponding FWHM value is of order 10% of t , is physically reasonable. The value of R_H is consistent with a good fit to the experimental data. As the value of E was refined, the value of phase shift per unit length, being energy dependent, had to be changed accordingly. These values were calculated, for polyethylene (C_2H_4 ; $\rho = 0.923 \text{ g/cm}^3$), using X-ray data from [27]. The agreement between the observed and calculated contrast and resolution values (see Table 5) is in general quite good, with the contrast values showing the expected peak as a function of R_l (with R being fixed), and the resolution values increasing monotonically.

The microfocus X-ray source was operated at a power of 1.5 W for which the manufacturer specifies that the source size is a minimum, nominally $4 \mu\text{m}$. It is also widely acknowledged that, because of the geometry of the target and the incident electron beam (target angle 22.5°), the effective X-ray spot as viewed along the optic axis is elliptical in shape. The disposition of the X-ray tube used here was such that the minor (major) axis of the ellipse was vertical (horizontal). The resolution of standard imaging plates has been estimated to be $150 \mu\text{m}$ FWHM at best (see e.g. [28]). Whilst the pixel size is determined by the raster-step size and the size of the laser focus in the imaging-plate scanner, the resolution is largely determined by the scattering of the laser beam inside the phosphor layer. The Fuji Imaging Plates that were used here were special plates developed for electron microscopy. The phosphor layer is thinner ($110 \mu\text{m}$) than for standard plates, which resulted in higher resolution (but lower sensitivity), and it contained a blue pigment which helped to reduce the scattering of the laser beam. Amemiya [29] has indicated that these plates have "a spatial resolution of slightly less than $100 \mu\text{m}$ ", in excellent agreement with the detector-parameter value obtained in Table 6. Finally, the effective X-ray energy (E) value given in Table 6 is entirely consistent with an X-ray tube operating at 30 kVp with minimal beam hardening from the tube window and object. In summary, the least-squares analysis has provided a good fit to experimental contrast and resolution data, and the refined-parameter values are all physically reasonable and in accord with expectations.

6. Conclusion

We have derived simple analytical expressions ("rules of thumb") for the maximum contrast, spatial resolution and signal-to-noise in the vicinity of the geometric image of a phase edge-like feature in a sample. The expressions depend on the sharpness of the edge and the maximum phase shift generated by the feature, as well as on the PSF of the imaging system, the source-to-object and object-to-detector distances, and the wavelength spectrum. The main factors determining the characteristics of the image are the maximum absolute phase shift, $|\varphi|_{\max}$, and the Fresnel number, $N_F = k\sigma_M^2 / R'$, which is defined with respect to the total variance σ_M^2 equal to the sum of the variance of the PSF of the imaging system, $\sigma_{\text{sys}}^2(M)$, and that of the unsharpness of the edge, σ_{obj}^2 . The spatial resolution behaves quite differently for large and small Fresnel numbers. In the case of large Fresnel numbers (short propagation distances) the spatial resolution is simply equal to the width of the PSF of the imaging system, $2\sigma_{\text{sys}}(M)$, while for small Fresnel numbers (large propagation distances) the resolution is equal to the width, $\sqrt{R'\lambda}$, of the first Fresnel zone. We showed that the contrast and the signal-to-noise are always directly proportional to the maximum absolute phase shift. At short effective propagation distances R' , when the corresponding Fresnel number is large, the maximum image contrast is inversely proportional to the Fresnel number, while at long propagation distances (small Fresnel numbers) the maximum contrast asymptotically tends to the limit $0.4876|\varphi|_{\max}$, which does not depend on any parameters other than the maximum absolute phase shift. The signal-to-noise behaves similarly, as it is proportional to the product of maximum image contrast and the square root of the integrated X-ray intensity incident on the sample feature that is being imaged. When the relevant Fresnel number is large, the expressions for the image contrast, spatial resolution and signal-to-noise in the case of polychromatic radiation are virtually the same as in the monochromatic case with the suitable replacement of the conventional phase by the generalized eikonal of the polychromatic beam. The behaviour is much more complicated in the case of small Fresnel numbers (large propagation distances) and polychromatic radiation, where we could not obtain simple and general analytical expressions for the image characteristics.

Acknowledgement

The authors are grateful to XRT Ltd for encouragement of this work.